Etching mechanisms of (In, Ga, Zn)O thin films in $CF_4/Ar/O_2$ inductively coupled plasma

Kwangsoo Kim, Alexander Efremov, Junmyung Lee, Kwang-Ho Kwon, and Geun Young Yeom

Citation: Journal of Vacuum Science & Technology A: Vacuum, Surfaces, and Films **33**, 031601 (2015);
View online: https://doi.org/10.1116/1.4913735
View Table of Contents: http://avs.scitation.org/toc/jva/33/3
Published by the American Vacuum Society

Etching mechanisms of (In, Ga, Zn)O thin films in $CF_4/Ar/O_2$ inductively coupled plasma

Kwangsoo Kim
Department of Electronic Engineering, Sogang University, Seoul 121-742, South Korea

Alexander Efremov
Department of Electronic Devices and Materials Technology, State University of Chemistry and Technology, 7 F. Engels St., 153000 Ivanovo, Russia

Junmyung Lee and Kwang-Ho Kwon[a)]
Department of Control and Instrumentation Engineering, Korea University, Sejong 339-700, South Korea

Geun Young Yeom
Department of Advanced Materials Science and Engineering, Sungkyunkwan University, Suwon 440-746, South Korea

(Received 12 May 2014; accepted 17 February 2015; published 26 February 2015)

The authors investigated the etching characteristics and mechanisms of (In, Ga, Zn)O (IGZO) thin films in $CF_4/Ar/O_2$ inductively coupled plasmas. The etching rates of IGZO as well as the IGZO/SiO_2 and IGZO/Al_2O_3 etching selectivities were measured as functions of O_2 content in a feed gas (0%–50%) and gas pressure ($p = 4$–10 mTorr) at fixed input power ($W_{inp} = 700$ W) and bias power ($W_{dc} = 200$ W). It was found that the IGZO etching rate decreases monotonically toward O_2 rich plasma but exhibits a maximum under gas pressure conditions. The zero-dimensional plasma model with Langmuir probe diagnostics data provided the information on plasma parameters and densities of plasma active species. The model-based analysis shows the dominance of the ion-flux-limited etching regime at $p \geq 6$ mTorr as well as the noticeable influence of CF_x radicals on the overall etching kinetics. © *2015 American Vacuum Society*. [http://dx.doi.org/10.1116/1.4913735]

I. INTRODUCTION

Recently, a lot of new materials have been studied to evaluate their potentialities for modern micro and nanoelectronics technology. Among these materials, there is the family of transparent conductive oxides (TCOs) used for electrodes in flat panel displays, solar cells, and organic light emitting diodes.[1] Initially, the dominant attention was attracted to the indium tin oxides $(In_2O)_n(SnO_2)_m$ (ITO).[2–4] The attractive properties of the ITO thin films were their low electrical resistivity and high optical transparency in the visible range of the spectrum.[4] Later, it was found that ZnO-based TCOs have advantages compared to ITO with nontoxicity, lower cost, and higher thermal and chemical stabilities.[5] Furthermore, it has been reported that the properties of the ZnO thin films can be effectively improved by some dopants, including In and Ga.[6,7] Therefore, development and optimization of the dry etch process for (In, Ga, Zn)O (IGZO) thin films is an important task to be solved to allow accurate pattern transfer and stable device parameters.

Most existing work on the etching characteristics of the ZnO-based TCOs relates to the undoped ZnO. The results can be summarized as follows:

(1) Hydrocarbon-based etching chemistries (CH_4, C_2H_6) provide the highest etching rates (up to 200 nm/min) due to the formation of highly volatile metal-organic compounds, but suffer from polymer deposition and degradation of the photoluminescence properties of the etched surface.[8,9]
(2) In chlorine-based (Cl_2, BCl_3) plasmas, the ZnO etching process occurs mostly in the ion flux-limited etching regime and is characterized by a relatively low etching rate (~80–90 nm/min).[10–12]
(3) Bromine-based (HBr) etching chemistry provides the lowest etching rate (~30–40 nm/min), while the etching process occurs in the reaction rate-limited etch regime with Br atoms acting as the main chemically active species.[13,14] The addition of even a small amount of fluorine-containing gas decreases the ZnO etching rate [by a factor of 3 at 15% CHF_3 in HBr (Ref. 14)]. The same etching mechanism was also found for the Ga-doped ZnO thin films.[15]

These features are in general agreement with the volatilities of reaction products, which can be characterized by their melting points (Fig. 1).

For the IGZO thin films, there are only few reports on their etching characteristics and mechanisms in Cl_2 and BCl_3 based plasmas.[16–18] In particular, it was found that BCl_3-based plasma provides higher IGZO etching rate compared with Cl_2-based plasmas, and the BCl_x radicals play the dominant role in the etching process. Also, the addition of O_2 to BCl_3 accelerates the IGZO etching process as has been repeatedly mentioned for many other oxide materials. The etching characteristics and mechanisms of IGZO thin films with fluorine-based gas chemistries have received little attention and, in fact, have not been explored in detail.

a)Electronic mail: kwonkh@korea.ac.kr

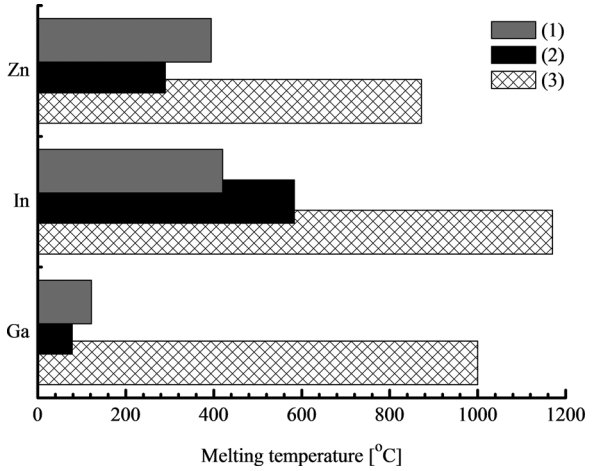

FIG. 1. Melting temperatures for saturated bromides (1), chlorides (2), and fluorides (3) of IGZO-forming metals.

In this work, we focused on investigating the etching characteristics and mechanisms for IGZO thin films with $CF_4/Ar/O_2$ gas chemistry. Our main goal was to understand how variations of gas mixing ratio and gas pressure influence the IGZO etching rate through the changes of internal plasma characteristics and composition. For this purpose, model-based analysis of plasma chemistry and etching kinetics was applied. Our interest in both SiO_2 and Al_2O_3 was due to their frequent use as the under- or overlaying layers in the IGZO-based devices. Therefore, these two materials were examined only to obtain the etching selectivity over IGZO. For both SiO_2 and Al_2O_3, the etching mechanism(s) in CF_4-based plasmas is not the key issue in this work because of much previous research.

II. EXPERIMENTAL AND MODELING DETAILS

A. Film preparation techniques

The IGZO thin films were deposited on thermally oxidized (300 nm) Si (100) substrate using radio frequency magnetron sputtering. The target was composed of In:Ga:Zn = 2:2:1 at. %. The process was performed in 8 sccm Ar + 2 sccm O_2 gas mixture at chamber pressure 0.75 mTorr and input power 400 W. The thickness of the IGZO films was ~100 nm. The film composition, determined by Auger analysis, was In:Ga:Zn:O at 19:18:8:55 atomic percentages, respectively.

B. Experimental setup and plasma diagnostics

Both etching and plasma diagnostics experiments were performed in a planar inductively coupled plasma (ICP) reactor. The reactor had a cylindrical ($r = 16$ cm) chamber made from anodized aluminum and a five-turns copper coil located above a 10 mm horizontal quartz window. The coil was connected to a 13.56 MHz power supply. The distance (l) between the window and the bottom electrode, used as a substrate holder, was 12.8 cm. The bottom electrode was connected to a 12.56 MHz power supply to maintain a negative dc bias voltage ($-U_{dc}$). The temperature of the bottom electrode was stabilized at 17 °C, using a water flow cooling system. The etched samples, ~2×2 cm^2, were placed in the center of the bottom electrode. Etched depths were measured using a surface profiler (Alpha-step 500, Tencor). For this purpose, we developed line striping of the photoresist (PR) (AZ1512, positive) with line width/spacing ratio 2 μm/2 μm. The initial thickness of the PR layer was ~1.5 μm.

Plasma diagnostics were measured by double Langmuir probe (LP) (DLP2000, Plasmart, Inc.). The probes were installed through the viewport on the sidewall of the reactor chamber at 5.7 cm above the bottom electrode and centered in a radial direction. The treatment of $I - V$ curves aimed at obtaining electron temperature (T_e) and ion saturated current density (J_+) was carried out using the software supplied by the equipment manufacturer. The calculations were based on Johnson and Malter double probe theory[19] with the one-Maxwellian approximation for the electron energy distribution function (EEDF). In order to obtain the total positive ion density (n_+) from the measured J_+, we used Allen–Boyd–Reynolds' approximation $J_+ \cong 0.61 e n_+ \upsilon$,[20] where $\upsilon \approx \sqrt{eT_e/m_i}$ is the ion Bohm velocity. The effective ion mass, m_i, was evaluated using Blank's law, assuming $y_i \sim k_{iz} y$, where y_i is the mole fraction of each ion inside n_+, k_{iz} is the ionization rate coefficient, and y is the mole fraction of the corresponding neutral particle.

To investigate the effects of O_2 mixing ratio, the experiments were performed at fixed total gas flow rate ($q = 40$ sccm), gas pressure ($p = 6$ mTorr), bias power ($W_{dc} = 200$ W), and input power ($W_{inp} = 700$ W). In Figs. 2, 4, and 6, the corresponding series of experiments (or model runs) are marked by label "1." The initial compositions of the $CF_4/Ar/O_2$ mixtures were set by adjusting the flow rates of the corresponding gases. In these experiments, the CF_4 flow rate q_{CF_4} was fixed at 20 sccm, while O_2 and Ar were mixed at various ratios within $q_{O_2} + q_{Ar} = 20$ sccm. Accordingly, the fraction of CF_4 in the initial gas mixture $y_{CF_4} = q_{CF_4}/q$ was always 0.5, and the remainder was represented by the different amounts of O_2 and Ar. The variation of O_2 content in a feed gas in the range of 0%–50% corresponds to the transition between CF_4/Ar and CF_4/O_2 gas systems.

To investigate the effects of gas pressure, we employed Ar rich (50% CF_4 + 38% Ar + 12% O_2) and O_2 rich (50% CF_4 + 12% Ar + 38% O_2) plasmas. In Figs. 2, 4, and 6, the corresponding series of experiments (or model runs) are marked by labels "2" and "3," respectively. The experiments were carried out for $p = 4$–10 mTorr at $q = 40$ sccm, $W_{dc} = 200$ W and $W_{inp} = 700$ W.

In all cases, each experimental point was reproduced for 5–7 times in order to control the experimental error. The relative error was ~10%–12% for the etching rate measurements and about ~3%–5% for the LP measurements.

C. Plasma modeling

To obtain data on densities and fluxes of plasma active species, we used a simplified zero-dimensional model with one-Maxwellian EEDF and the experimental data on T_e and n_+ as input parameters.[21,22] Such simplification for the CF_4

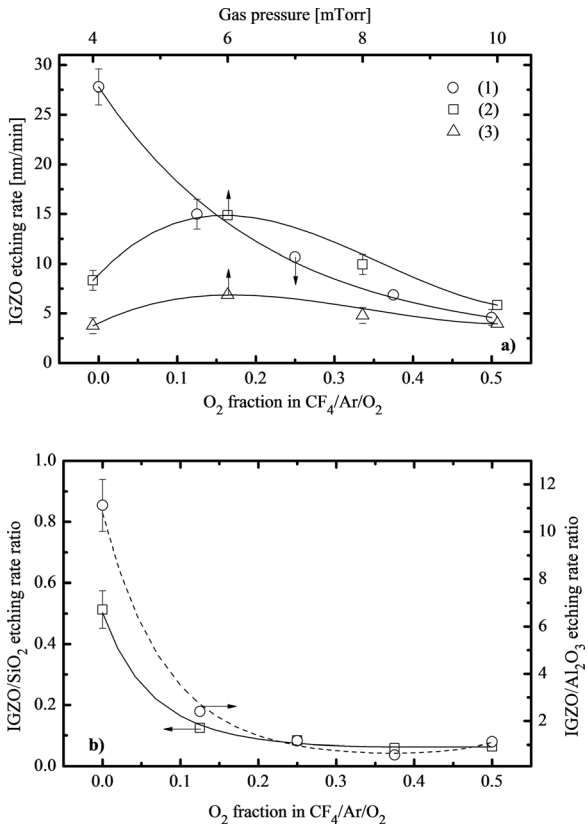

FIG. 2. IGZO etching rates (a) and selectivities (b) as functions of O_2 fraction in $CF_4/O_2/Ar$ gas mixture (1) and gas pressure [(2) and (3)]. Curve (1) corresponds to $p = 6$ mTorr at $q = 40$ sccm, $W_{inp} = 700$ W, and $W_{dc} = 200$ W. Curve (2) is for the Ar rich plasma (50% $CF_4 + 38\%$ Ar $+ 12\%$ O_2) at $q = 40$ sccm, $W_{inp} = 700$ W, and $W_{dc} = 200$ W. Curve (3) is for the O_2 rich plasma (50% $CF_4 + 12\%$ Ar $+ 38\%$ O_2) at $q = 40$ sccm, $W_{inp} = 700$ W, and $W_{dc} = 200$ W. The solid lines given by the cubic spline fitting of the experimental points are to guide the eye only.

based low-pressure ($p < 50$ mTorr) ICPs provides reasonable agreement between the plasma diagnostics and modeling.[22–24]

The electron density (n_e) was estimated from simultaneous solution of the steady-state ($dn/dt = 0$) equation of chemical kinetics for negative ions and the quasineutrality equation

$$n_e \approx \frac{k_{ii} n_+^2}{\sum_j k_{da,j} n_j + k_{ii} n_+}.$$

The rate coefficients of dissociative attachment k_{da} for neutral species with partial densities of n were taken from Refs. 25–27 as functions of T_e. The ion–ion recombination rate coefficient, $k_{ii} = 1 \times 10^{-7}$ cm^3/s, was assumed to be the same for all types of positive and negative ions.[26,27]

The steady-state densities of neutral species were obtained from the system of chemical kinetics equations in the general form $R_F - R_D = (k_s + 1/\tau_R)n$, where R_F and R_D are the volume averaged formation and decay rates in bulk plasma for a given species, k_S is the first order heterogeneous decay rate coefficient, and $\tau_R = \pi r^2 lp/q$ is the residence time. The list of processes included in the model is given in Table I. Compared with our previous work,[24] this table contains only those reactions with a principal influence on the particle balance for the given range of experimental conditions. The rate coefficients for electron impact reactions (R1–R16) were calculated using the fitting expressions $k = AT_e^B \exp(-C/T_e)$.[24–27] The rate coefficients for R17–R48 were taken from Bose *et al.*[26] and NIST chemical kinetics database[28] for the gas temperature (T) of 700 K. The last was assumed to be independent of the variable operating parameters. The rate coefficients for heterogeneous loss of atoms and radicals, R49–R55, were taken similarly to Ref. 21 as $k_S = [(\Lambda^2/D) + (2r/\gamma v_T)]^{-1}$, where D is the effective diffusion coefficient, γ is the sticking probability,[25,27] $\Lambda^{-2} = (2.405/r)^2 + (\pi/l)^2$ is the diffusion length, and $v_T = (8k_B T/\pi m)^{1/2}$. All reaction pathways between the adsorbed (marked by the s index) and gaseous species inside R49–R55 were assumed to be of equal probabilities. The rate coefficients for heterogeneous loss of ions R56 were calculated as $k_S = v/d_c$, where $d_c = 0.5rl/(rh_l + lh_r)$. The correction factors for axial, h_l, and radial, h_r, sheath sizes are given by low pressure diffusion theory.[29]

III. RESULTS AND DISCUSSION

A. Etching rates and selectivities

Figure 2(a) shows that an increase in O_2 fraction in a feed gas at constant chamber pressure results in the monotonic decrease in the IGZO etching rate from 27.8 to 4.6 nm/min for 0%–50% O_2. Therefore, the IGZO etching rate in the CF_4/O_2 gas system is reduced by a factor ~6 compared to that in the CF_4/Ar gas system. An increase in gas pressure in the range of 4–10 mTorr causes the nonmonotonic IGZO etching rates in both Ar rich and O_2 rich plasmas, with the maximum etching rates correspond to $p = 6$ mTorr. The relative heights of maxima in both Ar rich and O_2 rich plasmas are also quite close and occupy the range of 1.7–1.8 times compared with the etching rate corresponding to the lowest pressure end.

The etching rates of SiO_2 and Al_2O_3 exhibit weakly nonmonotonic behaviors with increasing O_2 mixing ratio. For both materials, the etching rates in the CF_4/O_2 gas system are significantly higher compared with those in the CF_4/Ar gas system, so that the IGZO/SiO_2 and IGZO/Al_2O_3 etching selectivities show deep (about an order of magnitude) falls toward more oxygenated plasmas [Fig. 2(b)]. Whereas the behaviors of both SiO_2 and Al_2O_3 etching rates versus gas pressure are similar to that for IGZO. Thus, the corresponding etching selectivities may be characterized by the constant averaged values.

B. Plasma parameters and densities of active species

Figure 3 presents the results of plasma diagnostics by Langmuir probes. Figure 3(a) shows that substitution of Ar for O_2 results in decreasing T_e in the range of 3.63–3.38 eV at $p = 6$ mTorr. This is due to an increase in the electron energy loss for the low-threshold excitations (vibrational, electronic) of O_2 and other molecular species, which appear in a gas phase as products of plasma chemical reactions. The similar behavior of T_e with increasing gas pressure

TABLE I. Reaction set for modeling of neutral species chemistry in $CF_4/O_2/Ar$ plasma. The rate coefficients for R1–R16 are from Refs. 24–27, for R17–R48 are from Refs. 26 and 28. The sticking probabilities for R49–54 are from Refs. 25 and 27. The units for rate coefficients of R1–R48 are cm^3/s.

		Rate coefficient (cm^3/s)			
	Process	ε_{th} (eV)	A	B	C
R1	$CF_4 + e = CF_3 + F + e$	5.60	1.38×10^{-8}	0	16
R2	$CF_4 + e = CF_2 + 2F + e$	9.50	2.22×10^{-10}	0.99	14.77
R3	$CF_4 + e = CF_3^+ + F + 2e$	15.9	9.36×10^{-8}	0	20.4
R4	$CF_3 + e = CF_2 + F + e$	3.80	6.48×10^{-8}	−0.959	11.25
R5	$CF_2 + e = CF + F + e$	5.40	8.11×10^{-9}	0.386	8.739
R6	$CF_2 + e = C + 2F + e$	11.00	1.39×10^{-8}	−1.164	49.87
R7	$CF + e = C + F + e$	5.60	1.63×10^{-8}	−0.002	13.05
R8	$F_2 + e = 2F + e$	4.34	1.08×10^{-8}	−0.296	4.464
R9	$O_2 + e = 2O + e$	6.40	1.52×10^{-9}	0	4.15
R10	$O_2 + e = O + O(1d) + e$	8.57	2.04×10^{-8}	0	8.18
R11	$CO_2 + e = CO + O + e$	13.50	1.87×10^{-8}	0	13.89
R12	$CO + e = C + O + e$	13.50	1.87×10^{-8}	0	13.89
R13	$O + e = O(1d) + e$	1.97	4.47×10^{-9}	0	2.29
R14	$FO + e = F + O + e$	4.30	6.16×10^{-9}	0	4.30
R15	$CFO + e = CO + F + e$	5.40	8.11×10^{-9}	0.386	8.739
R16	$CF_2O + e = CFO + F + e$	3.80	6.48×10^{-8}	−0.959	11.25
R17	$F_2 + CF_3 = CF_4 + F$		6.31×10^{-14}		
R18	$F_2 + CF_2 = CF_3 + F$		7.94×10^{-14}		
R19	$F_2 + CF = CF_2 + F$		3.98×10^{-12}		
R20	$F_2 + O(1d) = FO + F$		7.94×10^{-12}		
R21	$F_2 + CFO = CF_2O + F$		5.01×10^{-14}		
R22	$CF_3 + F = CF_4$		1.00×10^{-12}		
R23	$CF_3 + O = CF_2O + F$		3.16×10^{-11}		
R24	$CF_3 + O(1d) = CF_2O + F$		3.16×10^{-11}		
R25	$CF_2 + F = CF_3$		4.17×10^{-13}		
R26	$CF_2 + O = CFO + F$		3.16×10^{-11}		
R27	$CF_2 + O(1d) = CFO + F$		3.16×10^{-11}		
R28	$CF_2 + O = CO + 2F$		3.98×10^{-12}		
R29	$CF_2 + O(1d) = CO + 2F$		3.98×10^{-12}		
R30	$CF + F = CF_2$		5.01×10^{-15}		
R31	$CF + O = CO + F$		6.31×10^{-11}		
R32	$CF + O(1d) = CO + F$		2.00×10^{-11}		
R33	$CF + O_2 = CFO + O$		3.16×10^{-11}		
R34	$FO + O = F + O_2$		2.51×10^{-11}		
R35	$FO + O(1d) = F + O_2$		5.01×10^{-11}		
R36	$FO + FO = 2F + O_2$		2.51×10^{-12}		
R37	$2FO = F_2 + O_2$		2.51×10^{-16}		
R38	$CFO + CF_3 = CF_4 + CO$		1.00×10^{-11}		
R39	$CFO + CF_3 = CF_2O + CF_2$		1.00×10^{-11}		
R40	$CFO + CF_2 = CF_3 + CO$		3.16×10^{-13}		
R41	$CFO + CF_2 = CF_2O + CF$		3.16×10^{-13}		
R42	$CFO + O = CO_2 + F$		1.00×10^{-10}		
R43	$CFO + O(1d) = CO_2 + F$		1.00×10^{-10}		
R44	$2CFO = CF_2O + CO$		1.00×10^{-11}		
R45	$CFO + F = CF_2O$		7.94×10^{-11}		
R46	$CF_2O + O(1d) = F_2 + CO_2$		2.00×10^{-11}		
R47	$C + O_2 = CO + O$		1.58×10^{-11}		
R48	$CO + F = CFO$		1.29×10^{-11}		
R49	$F = F(s) + CF_3 = CF_4$ $+ CF_3 = CF_4$ $+ CF_2 = CF_3$ $+ CF = CF_2$ $+ F = F_2$ $+ C = CF$ $+ O = FO$		$f(\gamma), \gamma = 0.05$		
R50	$CF_3 = CF_3(s) + F = CF_4$		$f(\gamma), \gamma = 0.05$		

TABLE I. (*Continued*)

	Process	Rate coefficient (cm^3/s)			
		ε_{th} (eV)	A	B	C
R51	$CF_2 = CF_2(s) + F = CF_3$ $+ O = CF_2O$		$f(\gamma), \gamma = 0.1$		
R52	$CF = CF(s) + F = CF_2$ $+ O = CFO$		$f(\gamma), \gamma = 0.1$		
R53	$C = C(s) + F = CF$ $+ O = CO$		$f(\gamma), \gamma = 1$		
R54	$O = O(s) + O = O_2$ $+ F = FO$ $+ C = CO$ $+ CF = CFO$ $+ CF_2 = CF_2O$		$f(\gamma), \gamma = 0.1$		
R55	$O(1d) = O$		$f(\gamma), \gamma = 1$		
R56	$CF_3^+ = CF_3$		υ/d_c, where $\upsilon \approx \sqrt{eT_e/m_i}$, and $d_c = 0.5rl/(rh_l + lh_r)$		

(3.59–3.44 eV for Ar rich plasma and 3.45–3.33 eV for O_2 rich plasma at $p = 4$–10 mTorr) is also connected with increasing electron energy loss due to the increasing total density of neutral species and electron–neutral collision frequency. Figures 3(b) and 3(c) show that both J_+ and n_+ demonstrate a monotonic decrease toward O_2 rich plasmas at constant chamber pressure. As the composition of the feed gas changes from CF_4/Ar to CF_4/O_2, we obtain $n_+ = 4.88 \times 10^{10}$–$3.16 \times 10^{10}\,cm^{-3}$, which corresponds to $J_+ = 1.25$–$0.92\,mA/cm^2$. An increase in gas pressure from 4 to 10 mTorr also reduces the total density of positive ions for both Ar rich ($n_+ = 4.48 \times 10^{10}$–$4.16 \times 10^{10}\,cm^{-3}$) and O_2 rich ($n_+ = 3.47 \times 10^{10}$–$3.31 \times 10^{10}\,cm^{-3}$) plasmas. In all cases, the model-predicted electron density follows the behavior of n_+ while the gap between n_+ and n_e increases with more oxygenated plasmas and higher pressures. In our opinion, such effects are caused by a combination of two phenomena. First, a decrease in T_e suppresses the ionization through the decreasing ionization rate coefficients for all types of neutral species. The high sensitivity of ionization rate coefficients to T_e is due to $\varepsilon_{iz} \approx 12$–$15\,eV > (3/2)T_e$, where ε_{iz} is the threshold energy for ionization,[26,27] and $(3/2)T_e$ is the mean electron energy. Second, the substitution of Ar for O_2 as well as an increase in gas pressure, results in increasing densities of electronegative species due to both O_2 itself and oxygen-containing reaction products. This increases plasma electronegativity ($n_-/n_e = 0.14$–0.41 for 0%–50% O_2 at $p = 6$ mTorr, 0.13–0.32 for $p = 4$–10 mTorr in Ar rich plasma and 0.22–0.56 for $p = 4$–10 mTorr in O_2 rich plasma) and accelerates the decay for positive ions and electrons through ion–ion recombination and dissociative attachment, respectively.

Figure 4 illustrates the influence of O_2 content in the $CF_4/Ar/O_2$ gas mixture on the densities of neutral species. In the presence of oxygen, the F atom formation kinetics in electron-impact processes is noticeably influenced by several stepwise channels involving F_2 (R8), FO (R14), CFO (R15), and CF_2O (R16). The acceleration of R8 compared with the nonoxygenated plasmas is due to increasing F_2 density ($n_{F_2} = 6.84 \times 10^{11}$–$2.99 \times 10^{13}\,cm^{-3}$ for 0%–50% O_2), because of increasing formation rates in R46 and R49. The high density of FO (8.18×10^{10}–$6.23 \times 10^{12}\,cm^{-3}$ for 12%–50% O_2) is provided by a combined effect of R20, R49, and R54. The high formation rate for CFO species is supported by R16 and R48 while CF_2O is effectively formed in R39, R44, and R45. Furthermore, when the O_2 fraction in a feed gas exceeds 25% (i.e., $y_{O_2} > y_{Ar}$), the contribution of atom–molecular reactions R35–R37 and R42 to the F atom formation rate reaches the level of R14–R16. Consequently, in the 50% CF_4 + 50% O_2 gas mixture, the total effect from the electron-impact dissociations of reaction products (R8 and R14–R16) and atom–molecular reactions (R35–R37 and R42) exceeds the formation rate of F atoms due to the dissociation of CF_4 in R1–R3. As a result, though the efficiencies of all electron-impact reactions are slightly suppressed by decreasing T_e and n_e, the substitution of Ar for O_2 in the $CF_4/Ar/O_2$ gas mixture under the given process conditions provides a continuous increase in the total F atom formation rate and F atom density. The density of CF_3 radicals decreases toward O_2 rich plasmas due to increase decomposition rates in R23, R24 with the participation of O, O(1D) and in R38, R39, with the participation of CFO. Similar mechanisms result in decreasing densities for CF_2 and CF.

The behavior of F atom density versus gas pressure was found to be similar for both Ar rich ($n_F = 1.68 \times 10^{13}$–$4.01 \times 10^{13}\,cm^{-3}$ for $p = 4$–10 mTorr) and O_2 rich ($n_F = 2.83 \times 10^{13}$–$7.09 \times 10^{13}\,cm^{-3}$ for $p = 4$–10 mTorr) plasmas. The first case is mainly supported by increasing rates of R1–R3 and R14–R16 while in the second case the dominant role belongs to R14–R16 and R35–R37. The density of CF_x (x = 1–3) radicals in Ar rich plasma increases monotonically toward higher pressures (for example, $n_{CF_3} = 1.27 \times 10^{12}$–$2.29 \times 10^{12}\,cm^{-3}$ for $p = 4$–10 mTorr) following formation rates of these species in R1, R2, R4, and R5. In the highly oxygenated plasmas, this effect is overcompensated by the faster growth of decay frequencies of the CF_x species in the processes involving O, O(1D), and CFO. As a result, CF_x densities decrease monotonically

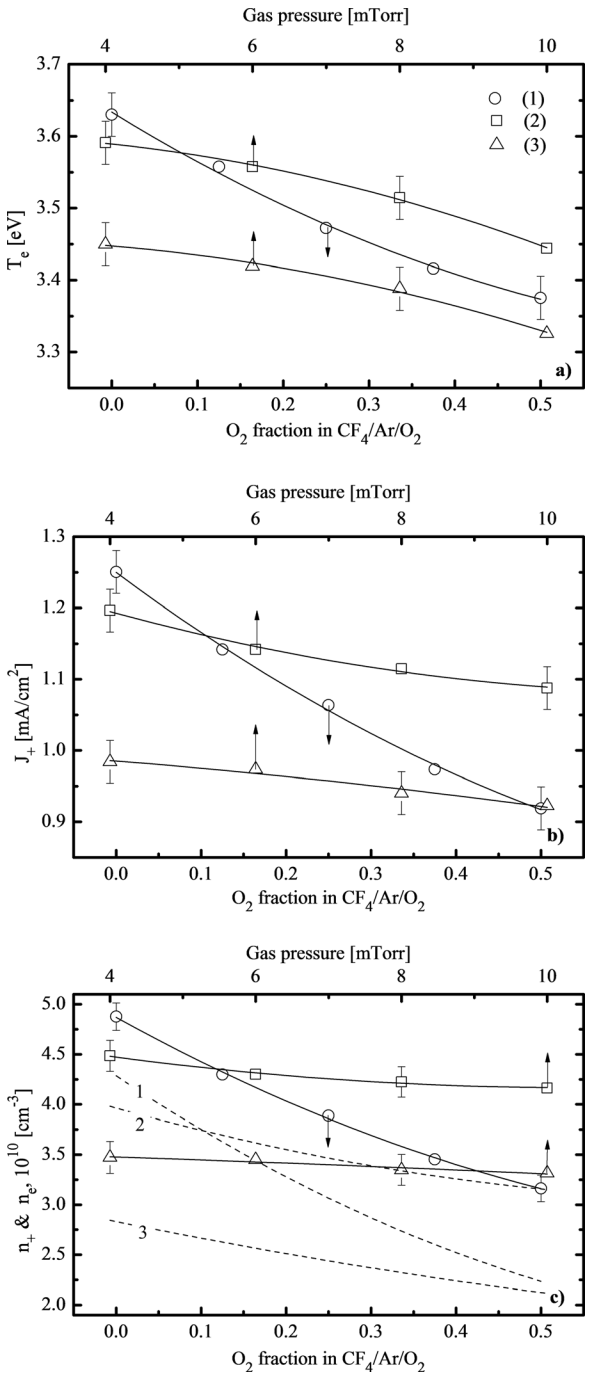

FIG. 3. Measured (solid lines + symbols) and model predicted (dashed lines) plasma parameters as functions of O_2 fraction in $CF_4/O_2/Ar$ gas mixture (1) and gas pressure [(2) and (3)]. The process conditions for the series of experiments or model runs labeled as 1, 2, and 3 correspond to Fig. 2. The solid lines given by the cubic spline fitting of the experimental points are to guide the eye only.

toward higher pressures (e.g., $n_{CF_3} = 1.92 \times 10^{10}$–$7.01 \times 10^9\,\mathrm{cm}^{-3}$ for $p = 4$–10 mTorr).

C. Etching mechanism approaches

It is well known that, when a chemically active gas is used for the etching process, the etching mechanism is determined by two main factors: the type of dominant active species and the volatility of reaction products. From Fig. 1, it can be understood that all IGZO-related metal fluorides are low volatile compounds. This allows one to neglect the spontaneous (thermally activated) desorption of reaction products and assume the IGZO etching mechanism to be the ion assisted chemical reaction. For further analysis, let us first account for the simplest situation with following assumptions:

(1) The main chemically active species are the fluorine atoms. Since all three oxide bonds are weaker than the fluoride ones (Fig. 5), a spontaneous chemical reaction between F atoms and IGZO-forming oxides at nearly room temperatures is possible. This means that the rate

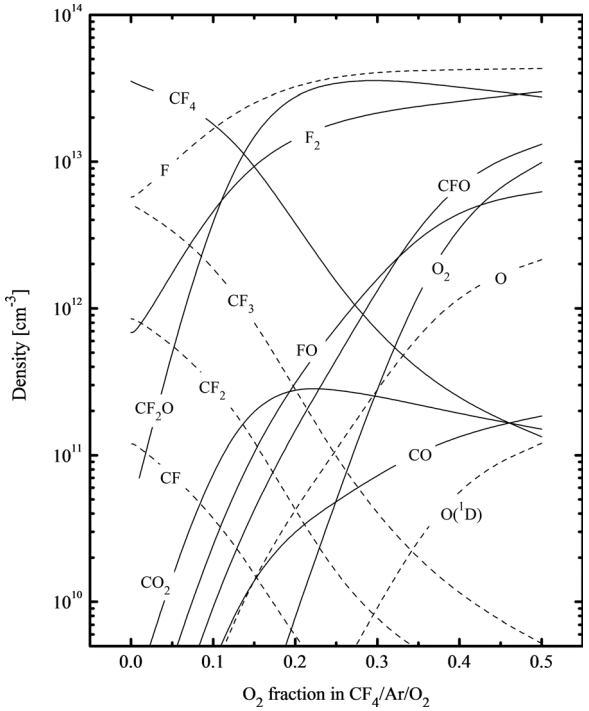

FIG. 4. Model predicted densities of neutral species as functions of O_2 fraction in $CF_4/O_2/Ar$ gas mixture. The process conditions for the series of experiments or model runs labeled as 1, 2, and 3 correspond to Fig. 2.

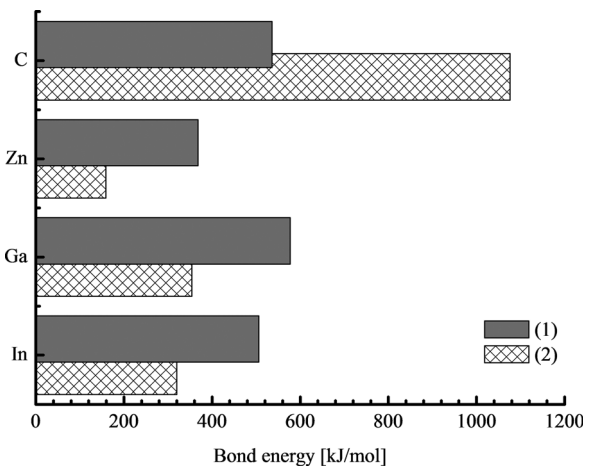

FIG. 5. Comparison of chemical bond energies in fluorides (1) and oxides (2) for IGZO-forming metals and carbon.

of chemical etching pathway is not limited by the ion-induced destruction of oxide bonds. Accordingly, it can be characterized by $\gamma_R\Gamma_F$,[30–32] where Γ_F is the flux of F atoms, and γ_R is the averaged reaction probability. For a given composition of reaction products, $\gamma_R = \text{const}$ at constant surface temperature.

(2) The main role of ion bombardment is the ion stimulated desorption of reaction products. The rate of this process is given by $Y_d\Gamma_+$,[30–32] where $\Gamma_+ \approx J_+/e$ is the total flux of positive ions on the etched surface, and Y_d is an averaged desorption yield. For ion bombardment energy $\varepsilon_i < 500\,\text{eV}$, one can assume $Y_d \sim \sqrt{\varepsilon_i}$.[32] Therefore, the rate of the physical etching pathway can be characterized by the parameter $\sqrt{\varepsilon_i}\Gamma_+$ (the ion energy flux), where $\varepsilon_i \approx e|-U_f - U_{dc}|$, and $U_f \approx 0.5T_e\ln(m_e/2.3m_i)$ is the floating potential.

(3) The etching mechanism is not affected by the fluorocarbon polymerization on the surface. This means that the thin steady-state (nonreactive)[33,34] fluorocarbon layer does not limit the transport of F atoms to the etched surface, and hence does not result in sufficient energy loss for ions. At the least, this same assumption will not disturb the good agreement between measured and model-predicted SiO_2 etching rates in $CF_4/Ar/O_2$ plasma under the close range of the experimental conditions.[24]

These allow one to consider the IGZO etching mechanism as a simple sequential two-step process

$$(\text{In, Ga, Zn})\text{O} + \text{F} \rightarrow (\text{In, Ga, Zn})\text{F} + \text{O}, \quad (1)$$

$$(\text{In, Ga, Zn})\text{F} + \text{ion} \rightarrow \text{desorbed}(\text{In, Ga, Zn})\text{F}. \quad (2)$$

Figure 6(a) shows that an increase in both O_2 fraction in the feed gas and gas pressure is accompanied by similar increasing tendencies for U_{dc} and thus, for ion bombardment energies ($\varepsilon_i = 235$–$274\,\text{eV}$ for 0%–50% O_2 at $p = 6$ mTorr, 254–263 eV for $p = 4$–10 mTorr in Ar rich plasma and 262–275 eV for $p = 4$–10 mTorr in O_2 rich plasma). However, this effect is overcompensated by decreasing Γ_+, so that a monotonic decrease in $\sqrt{\varepsilon_i}\Gamma_+$ toward more oxygenated plasmas and higher pressures occurs [Fig. 6(b)]. On the contrary, the fluxes of F atoms show a monotonic increase [Fig. 6(c)] following the densities of these species in a gas phase. The comparison of Figs. 2(a), 6(b), and 6(c) allows one to propose the IGZO etching mechanism as follows: It seems that for $p \geq 6$ mTorr, the ion bombardment does not provide effective cleaning of the etched surface from the reaction products. As a result, the IGZO etching process occurs in the ion-flux-limited etching regime, and the etching rate follows $\sqrt{\varepsilon_i}\Gamma_+$. For lower pressures, the etched surface is clean enough. Probably, such a condition is provided by the combination of lower fluorination rate and higher rate of ion-stimulated desorption. Here, the etching process occurs in the neutral-flux-limited mode, and the rate reflects the behavior of Γ_F. Therefore, the nonmonotonic change of the IGZO etching rate versus gas pressure results from the change of the process limiting condition from stages (1) to (2).

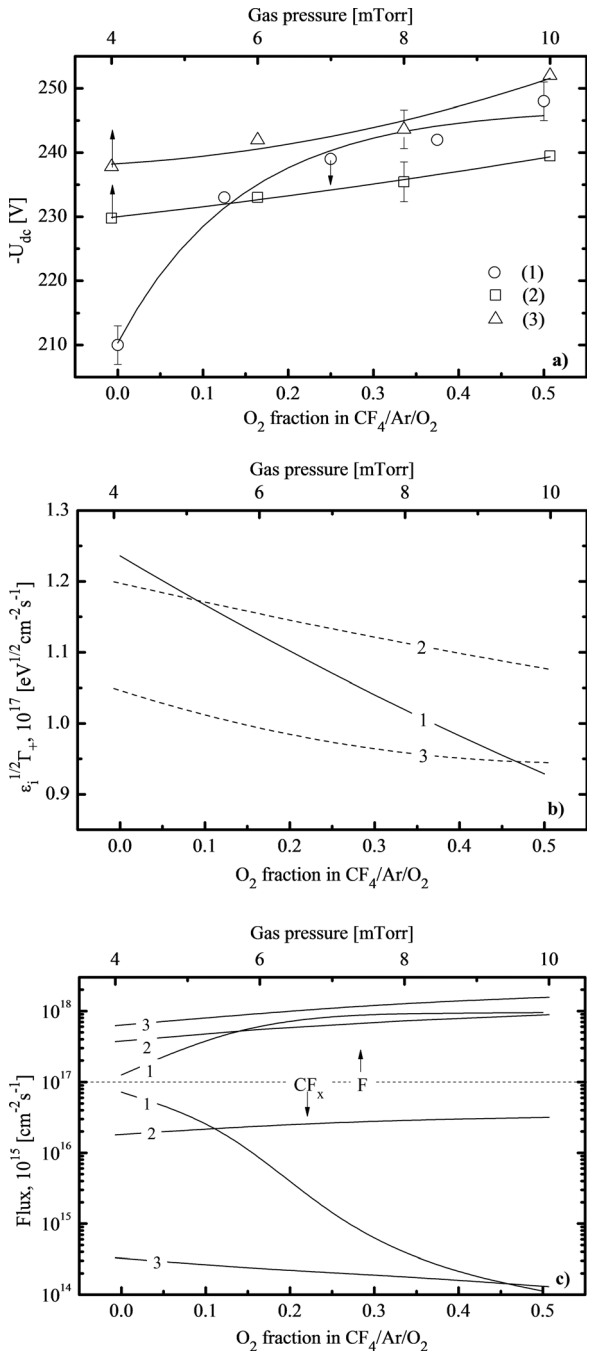

FIG. 6. Measured negative dc bias voltage (a), model predicted ion energy flux (b), and model predicted neutral species fluxes (c) as functions of O_2 fraction in $CF_4/O_2/Ar$ gas mixture (1) and gas pressure [(2) and (3)]. The process conditions for the series of experiments or model runs labeled as 1, 2, and 3 correspond to Fig. 2. In (a), the solid lines given by the cubic spline fitting of the experimental points are to guide the eye only. The term "CF_x" in (c) means the total flux of CF_3, CF_2, and CF.

Though the above explanation appears reasonable, it somewhat suffers from the quantitative disagreement between the changes of etching rate and ion energy flux. As the O_2 fraction in the $CF_4/Ar/O_2$ plasma increases from 0% to 50%, the IGZO etching rate decreases by a factor ~6, while $\sqrt{\varepsilon_i}\Gamma_+$ loses only 30% of its original value. To remove such inconsistency, we propose the following three

additional reaction pathways influencing the overall etching kinetics:

$$(\mathrm{In, Ga, Zn})\mathrm{O} + \mathrm{CF_x} \rightarrow \mathrm{COF_x} + (\mathrm{In, Ga, Zn}), \quad (3)$$

$$(\mathrm{In, Ga, Zn}) + \mathrm{CF_x} \rightarrow (\mathrm{In, Ga, Zn})\mathrm{CF_x}, \quad (4)$$

$$(\mathrm{In, Ga, Zn})\mathrm{CF_x} + \mathrm{ion} \rightarrow \mathrm{desorbed}\,(\mathrm{In, Ga, Zn})\mathrm{CF_x}. \quad (5)$$

The possibility of stage (3) at nearly room temperatures directly follows from the comparison of bond strengths in Fig. 5. The possibility of stage (4) is confirmed by the data of Kim *et al.*[35] where the authors have found $Zn(CF_x)$ compounds on the ZnO surface treated in CF_4/Ar plasma under a close range of experimental conditions. If one assumes a higher yield of ion-stimulated desorption for (In, Ga, Zn)CF_x compared with (In, Ga, Zn)F, the situation becomes clear. Since the fluxes of F atoms and CF_x radicals have opposite behaviors versus gas mixing ratio [Fig. 6(c)], an increase of O_2 fraction in a feed gas changes the composition of reaction products and leads to decreasing effective desorption yield. Therefore, the deep fall in the IGZO etching rate toward O_2 rich plasmas is probably provided by the simultaneous decrease of both multiplicands in $Y_d\Gamma_+$.

IV. CONCLUSION

In this work, we investigated etching characteristics and mechanisms of IGZO thin films in $CF_4/Ar/O_2$ inductively coupled plasmas. The variable parameters were the fraction of O_2, and hence Ar, in the feed gas and the gas pressure. It was found that the IGZO etching rate decreases monotonically toward O_2 rich plasma (27.8–4.6 nm/min for 0%–50% O_2), but exhibits a maximum versus gas pressure at $p = 6$ mTorr for both Ar rich and O_2 rich plasmas. To obtain the data on plasma parameters, densities, and fluxes of plasma active species needed for the analysis of the etching mechanism, we used a combination of plasma diagnostics from Langmuir probes and the zero-dimensional plasma model. The model-based analysis of etching kinetics showed the basic features of the IGZO etching mechanism to be as follows: (1) at $p \geq 6$ mTorr the etching process occurs in the ion-flux-limited etching regime, and (2) CF_x radicals have significant influence on the overall etching chemistry.

ACKNOWLEDGMENTS

This work was supported by the Industrial Strategic Technology Development Program (10041681, Development of fundamental technology for 10 nm process semiconductor and 10 G size large area process with high plasma density and VHF condition) funded by the Ministry of Knowledge Economy (MKE, Korea).

[1]H. Q. Chiang, J. F. Wager, R. L. Hoffman, J. Jeong, and D. A. Keszler, Appl. Phys. Lett. **86**, 13503 (2005).
[2]A. B. Djurisic, C. Y. Kwong, P. C. Chui, and W. K. Chan, J. Appl. Phys. **93**, 5472 (2003).
[3]H. Kupfer, R. Kleinhempel, B. Graffel, T. Welzel, T. Dunger, F. Richter, W. M. Gnehr, and T. Kopte, Surf. Coat. Technol. **201**, 3964 (2006).
[4]C. H. Jeong, J. H. Lee, J. T. Lim, M. S. Kim, and G. Y. Yeom, Surf. Coat. Technol. **201**, 5012 (2007).
[5]K. Ellmer, J. Phys. D: Appl. Phys. **34**, 3097 (2001).
[6]H. J. Ko, Y. F. Chen, S. K. Hong, H. Wenisch, and T. Yao, Appl. Phys. Lett. **77**, 3761 (2000).
[7]W. Lim, L. Voss, R. Khanna, B. P. Gila, D. P. Norton, S. J. Pearton, and F. Ren, Appl. Surf. Sci. **253**, 1269 (2006).
[8]J. M. Lee, K. M. Chang, K. K. Kim, W. K. Choi, and S. J. Park, J. Electrochem. Soc. **148**, G1 (2001).
[9]M. H. Shin, M. S. Park, S. H. Jung, J. H. Boo, and N. E. Lee, Thin Solid Films **515**, 4950 (2007).
[10]S. W. Na, M. H. Shin, Y. M. Chung, J. G. Han, S. H. Jeung, J. H. Boo, and N. E. Lee, Microelectron. Eng. **83**, 328 (2006).
[11]H. K. Kim, J. W. Bae, T. K. Kim, K. K. Kim, T. Y. Seong, and I. Adesida, J. Vac. Sci. Technol. B **21**, 1273 (2003).
[12]J. W. Bae, C. H. Jeong, H. K. Kim, K. K. Kim, N. G. Cho, T. Y. Seong, S. J. Park, I. Adesida, and G. Y. Yeom, Jpn. J. Appl. Phys. **42**, L535 (2003).
[13]Y.-H. Ham, A. Efremov, S. J. Yun, J. K. Kim, N.-K. Min, and K.-H. Kwon, Thin Solid Films **517**, 4242(2009).
[14]Y.-H. Ham, A. Efremov, H.-W. Lee, S. J. Yun, N. K. Min, K. Kim, and K.-H. Kwon, Jpn. J. Appl. Phys. **49**, 08JB03 (2010).
[15]Y.-H. Ham, A. Efremov, H. W. Lee, S. J. Yun, N. K. Min, K.-H. Baek, L.-M. Do, and K.-H. Kwon, Vacuum **85**, 1021 (2011).
[16]W. Park, K.-W. Whang, Y. G. Yoon, J. H. Kim, S.-H. Rha, and C. S. Hwang, Appl. Phys. Lett. **99**, 062110 (2011).
[17]Z. Yanbin, L. Guang, W. Wenlong, L. Xiuchang, and J. Zhigang, Plasma Sci. Technol. **14**, 915 (2012).
[18]K.-H. Kwon, A. Efremov, S. Kang, H. Jang, H. Yang, and K. Kim, Jpn. J. Appl. Phys. **51**, 076201 (2012).
[19]E. O. Johnson and L. Malter, Phys. Rev. **80**, 58 (1950).
[20]M. Sugavara, *Plasma Etching: Fundamentals and Applications* (Oxford University, New York, 1998).
[21]A. Efremov, N.-K. Min, B.-G. Choi, K.-H. Baek, and K.-H. Kwon, J. Electrochem. Soc. **155**, D777 (2008).
[22]A. M. Efremov, D.-P. Kim, and C.-I. Kim, Vacuum **75**, 133 (2004).
[23]T. Kimura and K. Ohe, Plasma Sources Sci. Technol. **8**, 553 (1999).
[24]J. Son, A. Efremov, I. Chun, G. Y. Yeom, and K.-H. Kwon, Plasma Chem. Plasma Process. **34**, 239 (2014).
[25]P. Ho, J. E. Johannes, R. J. Buss, and E. Meeks, J. Vac. Sci. Technol. A **19**, 2344 (2001).
[26]D. Bose, M. V. V. S. Rao, T. R. Govindan, and M. Meyyappan, Plasma Sources Sci. Technol. **12**, 225 (2003).
[27]T. Kimura and M. Noto, J. Appl. Phys. **100**, 063303 (2006).
[28]"NIST chemical kinetics database," http://kinetics.nist.gov/kinetics/index.jsp.
[29]M. A. Lieberman and A. J. Lichtenberg, *Principles of Plasma Discharges and Materials Processing* (John Wiley & Sons, Inc., New York, 1994).
[30]A. M. Efremov, D. P. Kim, and C. I. Kim, IEEE Trans. Plasma Sci. **32**, 1344 (2004).
[31]C. Lee, D. B. Graves, and M. A. Lieberman, Plasma Chem. Plasma Process. **16**, 99 (1996).
[32]H. F. Winters, J. W. Coburn, and T. J. Chuang, J. Vac. Sci. Technol. B **1**, 469 (1983).
[33]M. Schaepkens, T. E. F. M. Standaert, N. R. Rueger, P. G. M. Sebel, G. S. Oehrlein, and J. M. Cook, J. Vac. Sci. Technol. A **17**, 26 (1999).
[34]D. Zhang and M. J. Kushner, J. Vac. Sci. Technol. A **19**, 524 (2001).
[35]D. Kim, I. Hwang, J. Son, and H. Kim, J. Korean Phys. Soc. **58**, 1536 (2011).